PHOTONICS Research

Low-loss hybrid plasmonic TM-pass polarizer using polarization-dependent mode conversion

RUIXUAN CHEN,[1,2,3] BOWEN BAI,[1,2,3] AND ZHIPING ZHOU[1,2,3],*

[1]State Key Laboratory of Advanced Optical Communication Systems and Networks, Department of Electronics, School of Electronics Engineering and Computer Science, Peking University, Beijing 100871, China
[2]Peking University Shenzhen Research Institute, Shenzhen 518057, China
[3]Nano-optoelectronics Frontier Center of Ministry of Education, Peking University, Beijing 100871, China
*Corresponding author: zjzhou@pku.edu.cn

A low-loss hybrid plasmonic transverse magnetic (TM)-pass polarizer has been demonstrated utilizing polarization-dependent mode conversion. Taking advantage of the silicon hybrid plasmonic slot waveguide (HPSW), the unwanted transverse electric (TE) fundamental mode can be efficiently converted first to a TM higher-order mode and then suppressed by a power combiner, while the retained TM fundamental mode can pass through with negligible influence. Since the HPSW feature both strong structural asymmetry and a small interaction area in the cross-section between the metal and optical field, the optimized insertion loss of the device is as low as 0.4 dB. At the wavelength of 1550 nm, the extinction ratio is 28.3 dB with a moderate footprint of 2.38 μm × 10 μm. For the entire C band, the average reflection of the TE mode is suppressed below −14 dB, and the extinction ratio is over 18.6 dB. This work provides another more efficient and effective approach for better on-chip polarizers.   © 2020 Chinese Laser Press

https://doi.org/10.1364/PRJ.392654

1. INTRODUCTION

Driven by the urgent demand of applications in low cost, low power consumption and high-bandwidth interconnects, and the compatibility with complementary metal-oxide semiconductor (CMOS) processes, silicon photonics has been recognized as a promising technology to merge both optical and integrated circuits in a compact size and form new functional chips [1]. The intrinsic high-index-contrast in silicon waveguides results in compact size but also introduces strong polarization dependence. As a result, the silicon-based devices can only work well with either TE or TM polarization in general, and any decline in the purity of the operating polarization may cause serious performance degradation [2]. One common solution to tackle this problem is to deploy the polarization diversity scheme, in which polarization handling devices like polarization beam splitters (PBSs) [3–5] and rotators [6–8] are essential building blocks. In contrast with the increased complexity and system footprint that PBSs and rotators may bring, the on-chip polarizers offer another simple and effective approach to retain only one polarization in the system. On top of that, they also play vital roles in the applications of optical sensing [9] and communications [10].

Conventional on-chip polarizers [11–15], which are realized by dielectric schemes, normally result in a long device. For example, earlier work like Ref. [11] used a shallowly etched ridge

waveguide to form a TE-pass polarizer with a device length of 1 mm, and the consequent large footprint was not suitable for highly dense integration. For this reason, several types of silicon-based polarizers [16–20] have been proposed lately to shorten the device, but they have their own drawbacks. Polarizers based on photonic crystals [16,17] suffer from large insertion loss for the selected polarization and challenging fabrication process, while a subwavelength grating-based polarizer [18], which acts as a polarization-dependent Bragg reflector, is plagued by its large back-reflection. Although polarizers utilizing symmetric shallowly etched waveguides [19] and narrow waveguide section [20] appear to achieve both compact size (2.5 μm in Ref. [19] and 18 μm in Ref. [20]) and good performance, they are not based on the commonly used silicon-on-insulator (SOI) platform, where the typical Si layer thickness is 220 or 340 nm. Moreover, a unique idea using polarization-dependent resonant tunneling [21] has shown potential to achieve ultrashort device length (1.35 and 1.31 μm for TE-pass and TM-pass polarizers, respectively), but the additional silicon layer in the buried oxide layer is not realistic to be deposited by conventional SOI process.

As a promising approach to further increase the integration density of silicon photonic circuits, surface plasmon polaritons (SPPs) have shown great potential to realize ultracompact devices due to the unique properties of nanoscale optical field confinement [22]. Thus far, many hybrid plasmonic-based

polarizers have been demonstrated [23–30], but the large insertion loss is a big issue in that it may increase the output power requirement of the laser and the cost of thermal management on chip. The ordinary mechanism, e.g., introducing polarization-dependent loss [24–27], tends to make the device's cross-section have a large interaction area between the metal layer and optical field, which is the primary cause of the considerable loss. Alternatively, by adjusting cut-off conditions to shorten the interaction length (0.8 μm) [30], the insertion loss (0.88 dB) can be reduced but is still relatively large, let alone the difficult fabrication. Other mechanisms that are later applied, such as directional coupling [28] and Bragg effect [29], have been proven as effective approaches to achieve ultralow loss (<0.1 dB), but both of them have significant defects. As for the former, the long device length (30 μm) makes it lose the advantage of using SPPs; for the latter, the large reflection (−2.5 dB) is intolerable from a practical perspective. Despite these attempts to solve the big issue of large insertion loss, other appropriate methods need to be explored to achieve a real breakthrough.

In this paper, we present a low-loss hybrid plasmonic TM-pass polarizer based on polarization-dependent mode conversion. Taking advantage of the hybrid plasmonic slot waveguide (HPSW) as the core conversion component, strong structural asymmetry can be introduced with a small interaction area between the metal and optical field, so efficient TE_0-to-TM_1 conversion can be obtained in a compact region while not affecting the pass of TM fundamental mode. Any first higher-order mode produced in the conversion process will be further suppressed by the compact slot-to-strip mode convertor, which acts as a role of "power combiner," to avoid obvious reflection, and its energy will be scattered into the cladding. Unlike those possessing obvious defects or compromising the device size, this method can result in good comprehensive performance. The polarizer has a moderate footprint of 2.38 μm × 10 μm with a short active length of only 5.5 μm. At the central wavelength of 1550 nm, the insertion loss (IL) can be kept around 0.4 dB, while the extinction ratio (ER) is as high as 28.3 dB. In addition, the average reflection of TE mode is suppressed below −14 dB, and the bandwidth is approximately 65 nm when the extinction ratio is above 15 dB. This paper extends the idea of designing on-chip polarizers and paves the way toward practical use of hybrid plasmonic devices.

2. STRUCTURE AND WORKING PRINCIPLE

Figure 1(a) shows a schematic diagram of the proposed hybrid plasmonic TM-pass polarizer, which is based on the 340 nm SOI platform with SiO_2 upper cladding. The main body of the active region [inset (ii) in Fig. 1(a)] is constructed by the HPSW and is connected to the input and output single-mode strip waveguide with two strip-slot mode convertors [inset (i) in Fig. 1(a)]. As Fig. 1(b) depicts, the active region possesses a polarization-dependent mode-conversion process, which constitutes the design principle of the proposed device. When the TE fundamental mode (TE_0^{slot}) is launched into the active region, most of the output power will convert to TM first-order mode (TM_1^{slot}) with a little remaining in the TE_0^{slot}; for TM fundamental mode (TM_0^{slot}) incidence, it can
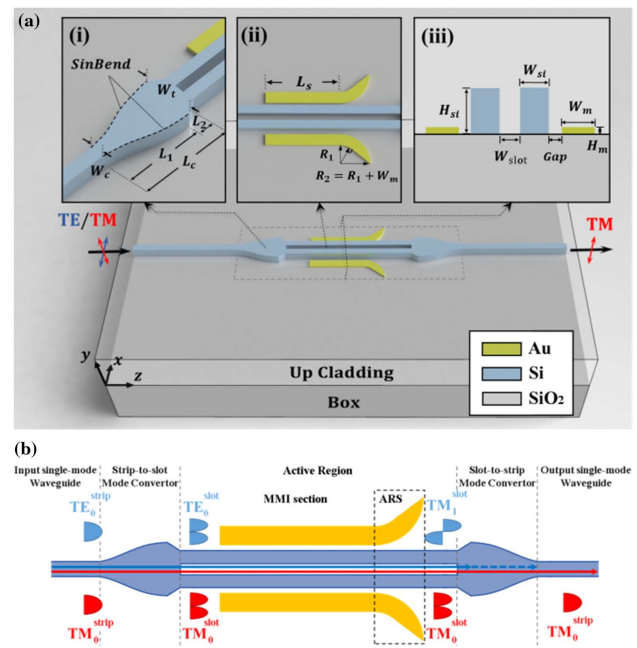

Fig. 1. (a) Schematic of the proposed TM-pass polarizer. Inset: (i) Compact strip-to-slot mode convertor; (ii) HPSW active region; (iii) cross-section of the HPSW. As an example, the widths of "rails" (W_{si}) and slot (W_{slot}) in the HPSW are chosen as 240 and 180 nm, while the width of metal layer (W_m) is chosen as 300 nm. Besides, the inner radius (R_1) and outer radius (R_2) of the metal "wing" in ARS are set as 500 and 800 nm in our design, respectively. Under this structural configuration, the dielectric slot waveguide supports four eigenmodes: TE_0^{slot}, TE_1^{slot}, TM_0^{slot}, and TM_1^{slot}. (b) The polarization-dependent mode-conversion process in the proposed device.

pass through the whole region with small propagation loss and only little optical power will convert to TE first-order mode (TE_1^{slot}). After that, the output slot-to-strip mode convertor functions as a "power combiner" to strip off any first higher-order modes. Thus, to function as a low-loss and high-ER TM-pass polarizer, the active region should feature both maximized TE_0^{slot}-to-TM_1^{slot} conversion and minimized TM_0^{slot}-to-TE_1^{slot} conversion. In addition, the strip-to-slot mode convertor should also ensure efficient coupling between the strip and slot waveguides for TM mode incidence. To further explain the above-mentioned polarization-dependent conversion process and fully understand the working principle of the device, both the active region and the strip-to-slot mode convertor are investigated in the following.

As shown in Fig. 1(b), the active region is composed of multimode interference (MMI) section and antireflection section (ARS). The former plays a central role in the mode-conversion process, while the latter is used to avoid the undesired reflection. The "MMI section" is formed by the HPSW, which can be regarded as a combination of dielectric slot and metal strip waveguides. Since they are close to each other, their field distribution will be coupled to form new eigenmodes. As illustrated in Figs. 2 and 3, there are six guided eigenmodes (EM_1–EM_6). The effect of the metal on the eigenmodes is not only reflected in the increasing number but also in the rotation of the optical axes. At the termination of the MMI
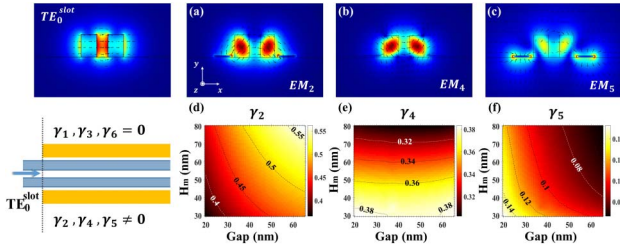
Fig. 2. Transverse magnetic-field profile of (a) EM_2, (b) EM_4, and (c) EM_5. Black arrows represent the electrical field directions. Corresponding power coupling ratios of (d) EM_2, (e) EM_4, and (f) EM_5 with sweeping Gap and H_m when TE_0^{slot} is injected into the HPSW. The mode profiles for TE_0^{slot}, EM_2, EM_4, and EM_5 are given under the dimension that $W_{si} = 240$ nm, $W_{slot} = 180$ nm, $W_m = 300$ nm, Gap = 45 nm, and $h_{Au} = 45$ nm.
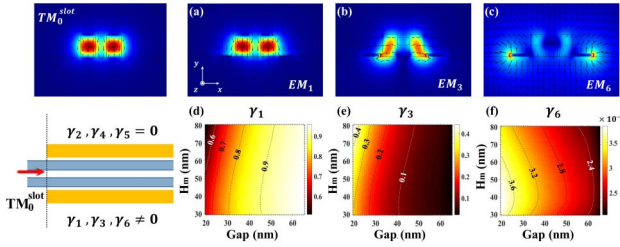

Fig. 3. Transverse magnetic-field profile of (a) EM_1, (b) EM_3, and (c) EM_6. Black arrows represent the electrical field directions. Corresponding power coupling ratios of (d) EM_1, (e) EM_3, and (f) EM_6 with sweeping Gap and H_m when TM_0^{slot} is injected into the HPSW. The mode profiles for TM_0^{slot}, EM_1, EM_3, and EM_6 are given under the dimension that $W_{si} = 240$ nm, $W_{slot} = 180$ nm, $W_m = 300$ nm, Gap = 45 nm, and $h_{Au} = 45$ nm.

section, the ARS constructed by a couple of metal "wings" is connected to avert the abrupt change of refractive index profile along the propagation direction (z axis). Moreover, the tips of the metal "wings" can efficiently prevent the optical power that coupled into the s-polarization mode in the metal strip from travelling back around its outer edge, which is another source causing undesired reflection. If we ignore the radiation modes, the incident TE_0^{slot} or TM_0^{slot} can be decoupled and rebuilt by the six guided eigenmodes in the MMI section. Although the plasmonic waveguide is a non-Hermitian system due to the losses of eigenmodes resulting from the metal layer, the six hybrid plasmonic eigenmodes still constitute a complete quasi-orthogonal space. Therefore, the optical field $\{\phi_{E_C}, \phi_{H_C}\}$ propagating in the MMI section can be expressed by

$$\phi_{E_C} = \sum_{i=1}^{6} a_i \phi_{Ei} \exp(-j\beta_i z), \tag{1}$$

$$\phi_{H_C} = \sum_{i=1}^{6} a_i \phi_{Hi} \exp(-j\beta_i z), \tag{2}$$

$$a_i = \frac{1}{4} \iint (\phi_{E_D} \times \phi_{Hi}^* + \phi_{Ei}^* \times \phi_{H_D})_{z=0} dS, \tag{3}$$

where $\{\phi_{E_D}, \phi_{H_D}\}$ and $\{\phi_{Ei}, \phi_{Hi}\}$ represent the normalized transverse electromagnetic field of the input dielectric mode (TE_0^{slot} or TM_0^{slot}) and the hybrid plasmonic eigenmodes (EM_i) propagating in the HPSW along the $+z$ direction with the complex propagation constant $\beta_i = n_{eff\,i}k_0$. The coupling coefficient for EM_i ($i = 1$–6) at the input facet of the HPSW ($z = 0$) can be calculated based on Eq. (3) and only hybrid plasmonic eigenmodes possessing identical modal symmetry with the incident dielectric mode can be excited. These calculations are conducted by extracting the mode profile data from Lumerical FDTD and conducting further numerical analysis in MATLAB. Therefore, for TE_0^{slot} incidence, only EM_2, EM_4, and EM_5 will be stimulated, and their power coupling ratios ($\gamma_i = |a_i|^2$) are depicted in Figs. 2(d)–2(f). These results indicate that more than 95% of the input power is coupled to these three eigenmodes, while EM_2 and EM_4 account for the majority (>78%). Because these three stimulated eigenmodes have a tilted electric field [black arrows shown in Figs. 2(a)–2(c)], they will beat with each other and accumulate phase shift while travelling through the HPSW. Similar to the self-imaging principles [31], the incident optical power, TE_0^{slot} mode, will be reconstructed into TM_1-like mode periodically along the propagation direction. If the MMI section is terminated at a nonspecific length, the output power will couple to TM_1^{slot} and TE_0^{slot}, which can be verified by mode similarity. For TM_0^{slot} incidence, as shown in Figs. 3(d)–3(f), most of the input power is coupled to the EM_1 due to its large mode similarity with TM_0^{slot}, while a little is coupled to the EM_3. In a similar way, the output power will be coupled to TM_0^{slot} and TE_1^{slot}. The proportion of γ_1 will rise to more than 90% when the metal layer moves as far as possible away from the silicon sidewall. Unlike eigenmodes having a tilted electric field, however, the optical axis of EM_1 and EM_3 remains almost the same as that of TM_0^{slot} and TE_1^{slot}. Hence, no mode beating will occur during their propagation in the HPSW.

On one hand, to maximize the TE_0^{slot}-to-TM_1^{slot} conversion efficiency, termination of the MMI section should be selected at half beat length (L_m), where the first destructive interference pattern of E_x appears. This length can be determined by calculating the mode-overlap ratio (Γ) between the TM_1-like mode on the termination facet and TE_0^{slot} in the output dielectric slot waveguide. This variable is used to evaluate the completeness of the TE_0^{slot}-to-TM_1^{slot} conversion. The smaller the value, the more complete the conversion from TE_0^{slot} to TM_1^{slot}:

$$\Gamma = 10 \log_{10} \frac{|\iint(\phi_{E_c} \times \phi_{H_D^{TE}}^* + \phi_{E_D^{TE}}^* \times \phi_{H_c})dS|^2}{\iint(\phi_{E_c} \times \phi_{H_c}^* + \phi_{E_c}^* \times \phi_{H_c})dS}. \tag{4}$$

For each swept parameter pair (Gap, H_m), only minimized Γ and its corresponding L_m will be recorded, and a 2D parameter space for these two figure of merits is plotted in Figs. 4(a) and 4(b). The smallest Γ is achieved when (Gap, H_m) is chosen as (35, 50) nm. Apart from this lowest point, other three extreme points [green stars shown in Figs. 4(a)], which are located at (30, 45) nm, (45, 45) nm, and (60, 30) nm, also have great potential to achieve efficient TE_0^{slot}-to-TM_1^{slot} conversion. On the other hand, the low-loss transmission of TM_0^{slot} should
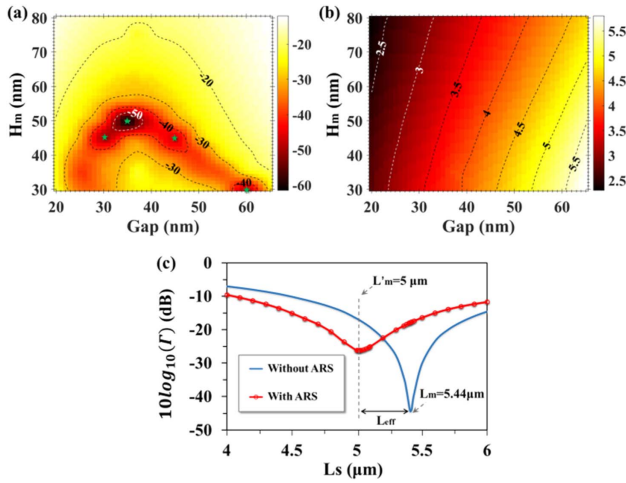
Fig. 4. (a) Mode overlap ratio after taking logarithm between the mode field on the termination facet of MMI section and TE_0^{slot} in the output dielectric slot waveguide. (b) Corresponding L_m with Gap and H_m varied. (c) Comparison between the mode overlap ratio with and without ARS.

Fig. 5. Insertion loss of the strip-to-slot mode convertor (IL_c) varied with respect to W_t (for TM_0 incidence). Inset: The transverse magnetic field evolution in the proposed strip-to-slot mode convertor and its schematic diagram of structural parameters.

also be realized simultaneously, and the conversion from TM_0^{slot} to TE_1^{slot} ought to be minimized. Thus, only (Gap, H_m) = (60, 30) nm is the most suitable choice, since Fig. 3(d) shows that both $\gamma_1 > 94\%$ and $\gamma_3 < 3\%$ can be achieved if the Gap is kept no less than 60 nm with H_m lower than 40 nm. Under this pair of parameter settings, the half beat length is $L_m = 5.44$ μm. However, this is not the final length of the MMI section in the real polarizer since the effective conversion length (L_{eff}) contributed from ARS has not yet been considered. So, to further determine the actual length of the MMI section (L_s), we employ the 3D finite-element-time-domain (FDTD) simulation to analyze the whole active region for TE_0^{slot} incidence by sweeping this structural parameter (L_s) and extract the mode-overlap ratio [red-dotted line in Fig. 4(c)] on the output facet of the dielectric slot waveguide. The comparison between the mode overlap ratios with and without ARS [Fig. 4(c)] shows that the sharp bend of ARS ($R_1 = 500$ nm) will provide an effective conversion length of 440 nm; thus, the actual length of the MMI section is only 5 μm. What is more, the shallower depth of the valley floor (red-dotted line) indicates that the existence of ARS will decrease the purity of the TM_1^{slot} in the output power, since the gradually increasing gap between silicon sidewall and sharp bend in the ARS will lead to the incomplete elimination of the E_x component.

3. LOW-LOSS HYBRID PLASMONIC TM-PASS POLARIZER

In the above section, the polarization-dependent mode-conversion process in the active region has been analyzed, and the optimized structure to realize both maximum TE_0^{slot}-to-TM_1^{slot} conversion and minimum TM_0^{slot}-to-TE_1^{slot} conversion has also been found. In order to minimize the insertion loss and the length of the whole polarizer, a low-loss and compact strip-to-slot mode convertor is also needed. Herein, we
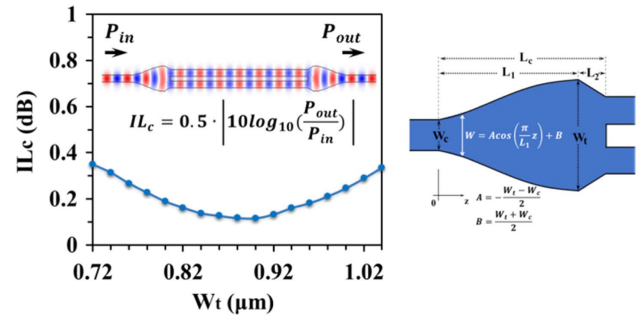
present a structure, as illustrated in Fig. 5. The width of the silicon waveguide W is increased sinusoidally along the propagation direction, so that the incident mode can be expanded smoothly and pass through the mode convertor in an adiabatic way. To simplify the analysis, we choose $L_c = 1.5$ μm and $L_2 = 0.2$ μm as an example to employ the following optimization for TM fundamental incidence. The insertion loss for a single strip-to-slot mode convertor (IL_c) is evaluated by the equation in the inset of Fig. 5, and a lowest value of approximately 0.1 dB can be achieved when W_t is selected as 0.89 μm.

To fully illustrate the concept, the entire polarizer is studied by employing the 3D FDTD method. To stabilize the converted mode, a certain length of dielectric slot waveguide is reserved before and after the active region, so that the final total length of the polarizer is 10 μm. The electric-field evolutions in the polarizer for both TE and TM fundamental mode incidence are demonstrated in Fig. 6. In particular, three key performance parameters are evaluated, including the extinction ratio ER [ER $= 10 \log_{10}(T_{out}^{TM}/T_{out}^{TE})$], insertion loss IL [IL $= |10 \log_{10}(T_{out}^{TM})| = |IL_{active} + 2IL_c|$], and reflection. T_{out}^X stands for the transmissivity of X-polarization ($X =$ TE or TM) after passing through the entire polarizer. The wavelength dependence of the transmissivity for both
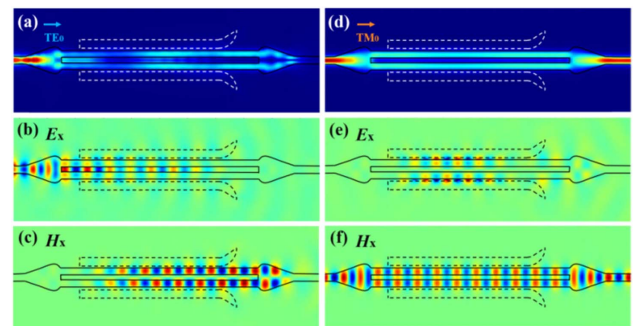

Fig. 6. Electric-field evolution with the corresponding (b), (e) E_x and (c), (f) H_x component in the proposed TM-pass polarizer for (a) TE and (d) TM fundamental input. The operation wavelength is 1550 nm, and the refractive indices for gold, SiO_2, and Si are $0.238 + 11.263i$ [32], 1.444, and 3.478, respectively. Besides, the minimum mesh of 5 nm in x, y, and z directions is set to obtain accurate and stable results.
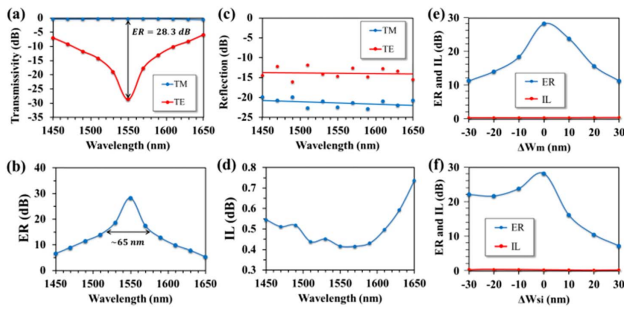
Fig. 7. Wavelength dependence of (a) transmissivity, (b) ER, (c) reflection, and (d) IL of the proposed device. ER and IL versus (e) ΔW_m and (f) ΔW_{si}.

polarization incidences is investigated in Fig. 7(a). The transmissivity for TM remains almost invariable across the entire wavelength range, while that for TE hits the bottom, which is about −28.7 dB, at the central wavelength of 1550 nm. Moreover, ER reaches the peak of 28.3 dB at the wavelength of 1550 nm, and the bandwidth of ER > 15 dB is about 65 nm. The average reflection for TE and TM fundamental incidence can be controlled below −14 dB and −22 dB, respectively, for the entire C band. The fluctuation of reflection comes from the fact that a small amount of reflection will be generated in the output slot-to-strip mode convertor from the diffraction process and then will result in the consequent resonance in the active region. The insertion loss for the whole device can be kept below 0.45 dB for the entire C band, while the loss induced by the active region is only 0.2 dB at 1550 nm. Finally, the fabrication tolerance of the ER and IL is shown in Figs. 7(e) and 7(f), which assumes that the central positions of both silicon and metal strips are accurate, while their widths W_{si} and W_m are changed by ΔW. The IL is not sensitive to the fabrication imperfection, while ER changes remarkably because the dimension deviations (ΔW_{si} and ΔW_m) have negligible influence on the mode similarity between TM_0^{slot} and EM_1 but change the optimal destructive interference condition for TE fundamental incidence. If ER > 15 dB is required, ΔW_m and ΔW_{si} should be controlled within the range of (−16, 20) nm and (−30, 10) nm, respectively.

4. CONCLUSION

In summary, we have demonstrated a low-loss hybrid plasmonic TM-pass polarizer based on HPSW structure. By using polarization-dependent mode conversion to convert and eliminate the unwanted polarization, the metal layer in the HPSW can provide strong structural asymmetry while maintaining small thickness of the metal layer that reduces its interaction area with the optical field. This trait of the idea guarantees that high extinction ratio (28.3 dB) and low loss (0.4 dB) can be realized simultaneously; further, it has also pushed the balance between footprint and performance of the plasmonic devices to a more realistic and competitive point. The same approach by using polarization-dependent mode conversion to design high-performance on-chip polarizers can be applied on other integration platforms.

REFERENCES

1. Z. Zhou, F. Yang, R. Chen, K. Zhu, P. Xu, and P. Sun, "Silicon photonics—a converging point of microelectronics and optoelectronics," Micro/Nano Electron. Intell. Manuf. **1**, 4–15 (2019).
2. H. Fukuda, K. Yamada, T. Tsuchizawa, T. Watanabe, H. Shinojima, and S. I. Itabashi, "Silicon photonic circuit with polarization diversity," Opt. Express **16**, 4872–4880 (2008).
3. X. Guan, H. Wu, Y. Shi, and D. Dai, "Extremely small polarization beam splitter based on a multimode interference coupler with a silicon hybrid plasmonic waveguide," Opt. Lett. **39**, 259–262 (2014).
4. B. Bai, Q. Deng, and Z. Zhou, "Plasmonic-assisted polarization beam splitter based on bent directional coupling," IEEE Photon. Technol. Lett. **29**, 599–602 (2017).
5. B. Bai, L. Liu, and Z. Zhou, "Ultracompact, high extinction ratio polarization beam splitter-rotator based on hybrid plasmonic-dielectric directional coupling," Opt. Lett. **42**, 4752–4755 (2017).
6. L. Liu, Y. Ding, K. Yvind, and J. M. Hvam, "Silicon-on-insulator polarization splitting and rotating device for polarization diversity circuits," Opt. Express **19**, 12646–12651 (2011).
7. L. Gao, Y. Huo, K. Zang, S. Paik, Y. Chen, J. S. Harris, and Z. Zhou, "On-chip plasmonic waveguide optical waveplate," Sci. Rep. **5**, 15794 (2015).
8. D. Dai and H. Wu, "Realization of a compact polarization splitter-rotator on silicon," Opt. Lett. **41**, 2346–2349 (2016).
9. L. Wu, J. Guo, H. Xu, X. Dai, and Y. Xiang, "Ultrasensitive biosensors based on long-range surface plasmon polariton and dielectric waveguide modes," Photon. Res. **4**, 262–266 (2016).
10. T. Barwicz, M. R. Watts, M. A. Popović, P. T. Rakich, L. Socci, F. X. Kärtner, E. P. Ippen, and H. I. Smith, "Polarization-transparent microphotonic devices in the strong confinement limit," Nat. Photonics **1**, 57–60 (2007).
11. D. Dai, Z. Wang, N. Julian, and J. E. Bowers, "Compact broadband polarizer based on shallowly-etched silicon-on-insulator ridge optical waveguides," Opt. Express **18**, 27404–27415 (2010).
12. Y. Xiong, D. Xu, J. H. Schmid, P. Cheben, and W. N. Ye, "High extinction ratio and broadband silicon TE-pass polarizer using subwavelength grating index engineering," IEEE Photon. J. **7**, 7802107 (2015).
13. H. Xu and Y. Shi, "On-chip silicon TE-pass polarizer based on asymmetric directional couplers," IEEE Photon. Technol. Lett. **29**, 861–864 (2017).
14. H. Zafar, P. Moreira, A. M. Taha, B. Paredes, M. S. Dahlem, and A. Khilo, "Compact silicon TE-pass polarizer using adiabatically-bent fully-etched waveguides," Opt. Express **26**, 31850–31860 (2018).
15. B. Ni and J. Xiao, "Subwavelength-grating-based compact and broadband TE-pass polarizer for slot waveguides on a SOI platform," J. Opt. Soc. Am. B **36**, 2126–2133 (2019).
16. D. W. Kim, M. H. Lee, Y. Kim, and K. H. Kim, "Ultracompact transverse magnetic mode-pass filter based on one-dimensional photonic crystals with subwavelength structures," Opt. Express **24**, 21560–21565 (2016).
17. C. Prakash and M. Sen, "Optimization of silicon-photonic crystal (PhC) waveguide for a compact and high extinction ratio tm-pass polarization filter," J. Appl. Phys. **127**, 023101 (2020).
18. X. Guan, P. Chen, S. Chen, P. Xu, Y. Shi, and D. Dai, "Low-loss ultracompact transverse-magnetic-pass polarizer with a silicon subwavelength grating waveguide," Opt. Lett. **39**, 4514–4517 (2014).
19. S. I. H. Azzam, M. F. O. Hameed, N. F. F. Areed, M. M. Abd-Elrazzak, H. A. El-Mikaty, and S. S. A. Obayya, "Proposal of an ultracompact CMOS-compatible TE-/TM-pass polarizer based on SOI platform," IEEE Photon. Technol. Lett. **26**, 1633–1636 (2014).
20. Q. Wang and S. Ho, "Ultracompact TM-pass silicon nanophotonic waveguide polarizer and design," IEEE Photon. J. **2**, 49–56 (2010).

21. S. I. Azzam and S. S. A. Obayya, "Ultra-compact resonant tunneling-based TE-pass and TM-pass polarizers for SOI platform," Opt. Lett. **40**, 1061–1064 (2015).

22. D. K. Gramotnev and S. I. Bozhevolnyi, "Plasmonics beyond the diffraction limit," Nat. Photonics **4**, 83–91 (2010).

23. Y. Huang, S. Zhu, H. Zhang, T.-Y. Liow, and G.-Q. Lo, "CMOS compatible horizontal nanoplasmonic slot waveguides TE-pass polarizer on silicon-on-insulator platform, " Opt. Express **21**, 12790–12796 (2013).

24. X. Sun, M. Z. Alam, S. J. Wagner, J. S. Aitchison, and M. Mojahedi, "Experimental demonstration of a hybrid plasmonic transverse electric pass polarizer for a silicon-on-insulator platform," Opt. Lett. **37**, 4814–4816 (2012).

25. M. G. Saber, N. Abadía, and D. V. Plant, "CMOS compatible all-silicon tm pass polarizer based on highly doped silicon waveguide," Opt. Express **26**, 20878–20887 (2018).

26. B. Bai, F. Yang, and Z. Zhou, "Demonstration of an on-chip TE-pass polarizer using a silicon hybrid plasmonic grating," Photon. Res. **7**, 289–293 (2019).

27. N. Abadía, M. G. Saber, F. Bello, A. Samani, E. El-Fiky, Y. Wang, J. F. Donegan, and D. V. Plant, "CMOS-compatible multi-band plasmonic TE-pass polarizer," Opt. Express **26**, 30292–30304 (2018).

28. X. Sun, M. Mojahedi, and J. S. Aitchison, "Hybrid plasmonic waveguide-based ultra-low insertion loss transverse electric-pass polarizer, " Opt. Lett. **41**, 4020–4023 (2016).

29. B. Bai, L. Liu, R. Chen, and Z. Zhou, "Low loss, compact TM-pass polarizer based on hybrid plasmonic grating," IEEE Photon. Technol. Lett. **29**, 607–610 (2017).

30. Z. Ying, G. Wang, X. Zhang, Y. Huang, H. Ho, and Y. Zhang, "Ultracompact TE-pass polarizer based on a hybrid plasmonic waveguide, " IEEE Photon. Technol. Lett. **27**, 201–204 (2015).

31. L. B. Soldano and E. C. M. Pennings, "Optical multi-mode interference devices based on self-imaging: principles and applications," J. Lightwave Technol. **13**, 615–627 (1995).

32. K. M. McPeak, S. V. Jayanti, S. J. P. Kress, S. Meyer, S. Iotti, A. Rossinelli, and D. J. Norris, "Plasmonic films can easily be better: rules and recipes," ACS Photon. **2**, 326–333 (2015).